*American Mineralogist, Volume 97, pages 1771–1782, 2012*

# Almandine: Lattice and non-lattice heat capacity behavior and standard thermodynamic properties

**Edgar Dachs,* Charles A. Geiger, and Artur Benisek**

Fachbereich Materialforschung and Physik, Abteilung Mineralogie, Universität Salzburg, Hellbrunnerstrasse 34, A-5020 Salzburg, Austria

## Abstract

The heat capacity of three synthetic polycrystalline almandine garnets (ideal formula $Fe_3Al_2Si_3O_{12}$) and one natural almandine-rich single crystal was measured. The samples were characterized by optical microscopy, electron microprobe analysis, X-ray powder diffraction, and Mössbauer spectroscopy. Measurements were performed in the temperature range 3 to 300 K using relaxation calorimetry and between 282 and 764 K using DSC methods. All garnets show a prominent λ-type heat-capacity anomaly at low temperatures resulting from a paramagnetic-antiferromagnetic phase transition. For two $Fe^{3+}$-free or nearly $Fe^{3+}$-free synthetic almandines, the phase transition is sharp and occurs at 9.2 K. Almandine samples that have ~3% $Fe^{3+}$ show a λ-type peak that is less sharp and that occurs at 8.0 ± 0.2 K. The low-$T$ $C_P$ data were adjusted slightly using the DSC results to improve the experimental accuracy. Integration of the low-$T$ $C_P$ data yields calorimetric standard entropy, $S°$, values between 336.7 ± 0.8 and 337.8 ± 0.8 J/(mol·K). The smaller value is recommended as the best $S°$ for end-member stoichiometric almandine, because it derives from the "best" $Fe^{3+}$-free synthetic sample.

The lattice (vibrational) heat capacity of almandine was calculated using the single-parameter phonon dispersion model of Komada and Westrum (1997), which allows the non-lattice heat capacity ($C_{ex}$) behavior to be modeled. An analysis shows the presence of an electronic heat-capacity contribution ($C_{el}$, Schottky anomaly) superimposed on a larger magnetic heat-capacity effect ($C_{mag}$) around 17 K. The calculated lattice entropy at 298.15 K is $S_{vib}$ = 303.3 J/(mol·K) and it contributes about 90% to the total standard entropy at 298 K. The non-lattice entropy is $S_{ex}$ = 33.4 J/(mol·K) and consists of $S_{mag}$ = 32.1 J/(mol·K) and $S_{el}$ = 1.3 J/(mol·K) contributions. The $C_P$ behavior for almandine above 298 K is given by the polynomial [in J/(mol·K)]:

$$C_P = 649.06(\pm4) - 3837.57(\pm122)\cdot T^{-0.5} - 1.44682(\pm0.06)\cdot10^{7}\cdot T^{-2} + 1.94834(\pm0.09)\cdot10^{9}\cdot T^{-3}$$

which is calculated using the measured DSC data together with one published heat-content datum determined by transposed-drop calorimetry along with a new determination in this work that gives $H_{1181K} - H_{302K}$ = 415.0 ± 3.2 kJ/mol.

Using our $S°$ value and the $C_P$ polynomial for almandine, we derived the enthalpy of formation, $\Delta H_f°$, from an analysis of experimental phase equilibrium results on the reactions almandine + 3rutile = 3ilmenite + sillimanite + 2quartz and 2ilmenite = 2Fe + 2rutile + $O_2$. A $\Delta H_f°$ = –5269.63 kJ/mol was obtained.

**Keywords:** Almandine, heat capacity, standard entropy, thermodynamics, standard enthalpy of formation, magnetic entropy, Schottky anomaly

## Introduction

Almandine garnet, ideally $Fe_3Al_2Si_3O_{12}$, is an important rock-forming silicate. As such it has received considerable thermodynamic study over the years using phase-equilibrium experimentation, electrochemical measurements and by means of calorimetry. More recently, lattice-dynamic calculations, both theoretically and experimentally based, have been used to calculate thermodynamic properties. Compilations of almandine's standard thermodynamic properties can be found in several different sources (e.g., Berman 1988; Chatterjee et al. 1998; Gottschalk 1997; Holland and Powell 1998, 2011) and were reviewed and evaluated by Geiger (1999). Over time, more accurate and precise thermodynamic as well as physical property values have emerged (e.g., compressibility, thermal expansion).

There are also several reports on the magnetic and electronic behavior of almandine deriving from the presence of $Fe^{2+}$ at the dodecahedral **E**-site (e.g., Prandl 1971; Murad and Wagner 1987; Anovitz et al. 1993; Geiger and Rossman 1994; Zherebetskyy et al. 2012). All physical properties are ultimately related to the crystal chemistry of almandine and, here, the bonding and vibrational behavior of $Fe^{2+}$ is important. Indeed, the **E**-site cations of all silicate garnets play a central role in determining their physical property behavior and they are thus receiving much current attention (see reviews of Geiger 2004, 2008). Several aspects still need further experimentation, especially at

* E-mail: edgar.dachs@sbg.ac.at

0003-004X/12/0010–1771$05.00/DOI: http://dx.doi.org/10.2138/am.2012.4163

low temperatures. Almandine undergoes an antiferromagnetic phase transition at roughly 8 K (Prandl 1971; Murad and Wagner 1987; Anovitz et al. 1993), but its precise contribution to thermodynamic properties is not understood quantitatively, nor is the effect of octahedral $Fe^{3+}$ on, for example, the Néel temperature. Recent low-temperature $C_P$ studies on several $Fe^{2+}$-containing silicate minerals (Dachs et al. 2007; Dachs and Geiger 2008) have shown, moreover, the presence of low-energy electronic transitions arising from spin-orbit interactions. Calorimetric investigations are essential in terms of investigating these magnetic and electronic effects. In terms of experimentation, one issue in older studies concerns the composition and structural state of synthetic almandine samples, as well as any possible impurity phases (Geiger et al. in prep.). This general issue has recently been discussed for the case of grossular garnet, which has also received much analysis regarding its precise thermodynamic properties (Dachs et al. 2012).

In addition to the study of macroscopic properties, mineral physics research on the lattice-dynamic behavior of relatively complex silicates is now being done and, here, almandine is no exception. Several investigations have been carried out (Pilati et al. 1996; Grammaccioli and Pilati 2003; Mittal et al. 2000; Chopelas 2006). Based on lattice dynamic calculations using empirical potentials (Pilati et al. 1996; Grammaccioli 2002; Grammaccioli and Pilati 2003), there are repeated claims, for example, that there is an order-disorder transition involving $Fe^{2+}$ around 100 K and/or static subsite disorder at the **E**-site in almandine (as well for **E**-site cations in other garnets). This has been claimed despite previously published diffraction and spectroscopic results, as well as low-temperature heat capacity measurements (Anovitz et al. 1993), that give no indication for any order/disorder transitions or static sub-site disorder (see reviews of Geiger 2004, 2008).

In this report, we present a set of systematic and detailed low- and high-temperature calorimetric $C_P$ measurements on almandine. $C_P$ behavior is analyzed with respect to the nature of phonon, magnetic, and electronic effects. The standard thermodynamic properties of almandine are calculated and are compared to those in the literature and its lattice-dynamic properties, derived from various published models, are critically analyzed.

## Samples and experimental methods

### Samples

The samples studied calorimetrically include three synthetic almandines labeled R41, R22, and R51 and one natural almandine-rich single-crystal, FR3. Sample R41 was synthesized following Geiger et al. (1987). An almandine glass was converted to crystalline garnet in a graphite crucible at 27 Kb and 1150 °C in a piston-cylinder apparatus. An X-ray powder measurement of the synthetic product showed only almandine peaks. Very fine Fe-metal grains <2 μm in size could be identified in backscattered electron photos made with the electron microprobe. Their amount is very minor and is estimated at <1 vol%. The composition of the sample from electron microprobe analysis is given in Table 1. Its $^{57}$Fe Mössbauer spectrum is shown in Figure 1. The measurements show that this almandine has little if any octahedral $Fe^{3+}$ and that it is very close to stoichiometric almandine composition.

Sample R22 was synthesized in two steps. First, two separate almandine samples were synthesized from a glass, which was different than that used for the synthesis of R41, but at the same *P-T* conditions. The two resulting almandines were put together in an agate mortar and intimately ground. The resulting material was rerun at 27 Kb and 1150 °C in a graphite crucible. Based on an X-ray powder measurement, only almandine peaks could be identified. Rare fine-grained and irregularly shaped hercynite grains about 5 μm in size could be indentified in backscattered electron photos. The amount is very minor and is estimated at 1 vol% or less. Based on electron microprobe analyses, the sample appears to have a minor andradite component (Table 1). A Mössbauer spectrum shows some octahedral $Fe^{3+}$ amounting to roughly 5 atomic percent of the total iron.

Sample R51 is an almandine synthesized from an oxide and Fe-metal mixture at high pressures and temperatures in a graphite crucible in a piston-cylinder apparatus (Geiger et al. in prep.). Back-scattered electron (BSE) photos and electron microprobe analyses show that the sample consists largely of almandine, but it contains some fine-grained unreacted or partially reacted starting material and other phases. Approximately 94–95 vol% of the sample consists of almandine and about 1–2% quartz, 1% Fe metal and 1–2% slightly aluminous ferrosilite were observed. An X-ray powder pattern shows only the strongest reflection for quartz at 26.6 2Θ (Cu$K_\alpha$). A Mössbauer spectrum shows the presence of very minor amounts of octahedral ferric iron.

**Table 1.** Electron microprobe results on almandine samples in terms of oxides and cations (based on 12 O atoms) and in terms of mole percents of various garnet end-members

| Oxides | R41 | R22 | R51 | FR3 |
|---|---|---|---|---|
| $SiO_2$ | 37.01(34) | 36.50(25) | 36.40(40) | 37.22(15) |
| $TiO_2$ | – | – | – | 0.02(3) |
| $Al_2O_3$ | 20.69(17) | 20.30(21) | 20.79(26) | 20.34(11) |
| FeO | 43.71(63) | 43.35(29) | 45.00(64) | 43.29(34) |
| MnO | – | – | – | 0.05(4) |
| MgO | – | – | 0.03(3) | 0.61(8) |
| CaO | 0.01(1) | 0.34(8) | – | 1.04(14) |
| Sum | 101.42(73) | 100.49(36) | 102.22(79) | 102.57(33) |
| **Cations*** | | | | |
| Si | 3.02 | 3.01 | 2.95 | 2.99 |
| Ti | – | – | – | – |
| Al | 1.99 | 1.97 | 1.99 | 1.92 |
| $Fe^{2+}$ | 2.99 | 2.98 | 2.95 | 2.83 |
| $Fe^{3+}$ | – | 0.01 | 0.10 | 0.08 |
| Mg | – | – | – | 0.07 |
| Ca | – | 0.03 | | 0.09 |
| Total | 8.00 | 8.00 | 7.99 | 7.98 |
| **Mole percent end-member*** | | | | |
| Almandine | 99.51 | 98.62 | 96.99 | 93.50 |
| Pyrope | – | – | 0.12 | 2.44 |
| Grossular | – | – | – | 0.00 |
| Spessartine | – | – | – | 0.11 |
| Andradite | – | 0.49 | | 2.93 |
| Skiagite | – | – | 1.35 | 0.77 |
| Schorlomite | – | – | – | 0.06 |
| Remainder | 0.46 | 0.90 | 1.54 | 0.18 |
| Total | 99.97 | 100.01 | 100.00 | 99.99 |

*Note:* Numbers in parentheses are one standard deviation and refer to the last digits.
* Calculated using the program of Locock (2008); skiagite: $Fe_3Fe_2Si_3O_{12}$, schorlomite-Al = $Ca_3Ti_2(SiAl_2)O_{12}$.

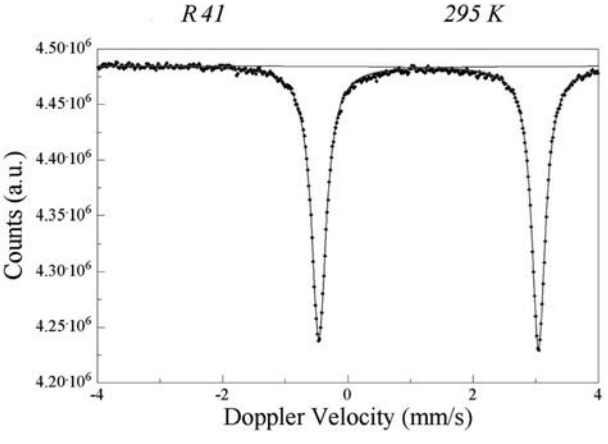


**Figure 1.** $^{57}$Fe Mössbauer spectrum of almandine R41.

Sample FR3 is a natural nearly end-member almandine found in an iron formation (Woodland et al. 1995). These garnets occur as fractured, reddish-brown crystals up to a couple of centimeters in size. In backscattered electron photos, a single inclusion of magnetite about 5–10 µm in size was found in our crystal used for calorimetry and also a second unidentifiable phase about 5 µm or less in size could be identified. It occurs in fine fractures. The total amounts of the two inclusion phases are minor and are estimated around 1–2 vol% of the crystal. No compositional zoning was detected in line traverses made using the electron microprobe. The composition of FR3 is given in Table 1.

Further discussion on the synthesis of almandine, its characterization and detailed crystal-chemical properties are discussed in Geiger et al. (in preparation). For calorimetric measurements, all samples were prepared as small well-polished platelets/chips that weighted between 17.4 and 29.8 mg.

## Low-temperature calorimetry

Low-temperature (i.e., 3 to 300 K) heat capacity was measured with the Physical Properties Measurement System (PPMS) constructed by Quantum Design (e.g., Lashley et al. 2003; Dachs and Bertoldi 2005). Heat capacity was measured at 60 different temperatures and three times at each temperature on cooling from 300 K with a logarithmic spacing. Around the prominent magnetic anomaly, a closer linear temperature spacing of 0.15 K was used. A complete PPMS experiment to measure $C_P$ comprises an "addenda run" and a "sample run." The first measurement determines the heat capacity of the empty sample platform plus Apiezon N grease that facilitates thermal contact between the platform and the sample. In the second measurement, the sample is placed on the platform and the heat capacity of the whole ensemble is measured. The net heat capacity of the sample is then given by the difference between the two measurements. The samples were directly mounted onto the sample platform via a polished surface. This provides for good sample coupling during a PPMS measurement (Dachs et al. 2010a). Sample coupling is defined as the ratio $100K_g/(K_g+K_w)$, where $K_g$ is the thermal conductance between the sample and the sample platform and $K_w$ is the thermal conductance of the wires that attach the sample platform to the puck frame (see Hwang et al. 1997; Lashley et al. 2003; Dachs and Bertoldi 2005 for more details). The closer the sample-coupling value is to 100%, the better the thermal conductance between sample platform and sample. This ensures a more robust heat capacity determination. The $C_P$ measurements were repeated three times to ensure good experimental reproducibility (Table 2).

## Differential scanning calorimetry (DSC)

Heat capacity was measured between 282 and 764 K with a Perkin Elmer Diamond DSC. Each $C_P$ determination consists of three separate measurements of a blank, a reference and a sample measurement. Before every sample measurement, the DSC was calibrated with a reference run using a synthetic single crystal of corundum of mass 31.764 mg. Its heat capacity values were taken from a National Bureau of Standards Certificate (Ditmars et al. 1982). Each almandine sample (a loose polycrystalline powder or a single-crystal contained in an Al pan and covered with a lid) was measured three to five times in this manner. The mean and standard deviation of these data gave $C_P$ and $\sigma_{C_P}$ for one experimental series. Two (for sample R51 three) different DSC mounts for each almandine were prepared to obtain two (for R51 three) independent DSC data sets per sample.

The DSC measurements were performed under a flow of Ar gas and the calorimeter block was kept at a constant temperature of 243.3 K using a Perkin Elmer Intracooler. A flow of dried air prevented the growth of ice crystals on the calorimeter block (the flow was set to 200 mL/min and the cover heater was turned off). The heat-flow data were collected in step-scanning mode with a heating rate of 10 K/min with temperature intervals of 100 K. The heat capacity of the blank run was subtracted from that of the reference and sample measurement, respectively, following the method described in Mraw (1988) and using a self-written Mathematica program. The final accuracy of the $C_P$ data is better than 0.6% applying this experimental procedure and the described DSC instrumental settings (Dachs and Benisek 2011).

## Transposed-drop calorimetry

The heat content of natural almandine FR3, when heated from 302 to 1181 K ($H_{1181}$–$H_{302}$), was measured in four transposed-drop-calorimetry experiments with a Calvet-type twin calorimeter as described by Cemic and Kähler (2000). The sample of mass ~100 mg was enclosed in a gold capsule (500 mg), which, after evacuation and filling with Ar gas, was welded shut. The calorimeter was calibrated using synthetic corundum, which was also enclosed in a gold capsule to achieve the same drop characteristics as in the sample run. The heat capacity of the Au capsule was calculated using the data in Hultgren et al. (1973). This calorimeter has a precision of ~3% for high-temperature heat of solution experiments (Benisek et al. 2003; Benisek et al. 2007). The drop experiments performed here generated thermal peaks about 10 times larger than those of solution experiments. Consequently, the precision of the drop experiments is ~0.3%.

## Data evaluation and treatment

**Treatment of the raw low-temperature heat capacity data.** The raw low-$T$ $C_P$ data measured on the synthetic polycrystalline almandines R41, R22, and R51 were "DSC adjusted," based on the repeated PPMS and DSC measurements, according to the method described in Dachs and Benisek (2011), as given by

$$(C_P^{\mathrm{PPMS}})_{\mathrm{adjusted}} = (C_P^{\mathrm{PPMS}})_{\mathrm{measured}}(C_P^{\mathrm{DSC}}/C_P^{\mathrm{PPMS}})^{298\mathrm{K}}. \quad (1)$$

The term $(C_P^{\mathrm{DSC}}/C_P^{\mathrm{PPMS}})^{298\mathrm{K}}$ is a factor typically lying between 1.000 and 1.011 and a value >1.0 indicates that the PPMS $C_P$ data were adjusted to slightly higher values. The application of Equation 1 to all possible combinations of the PPMS and DSC heat capacity data sets resulted in six to nine adjusted PPMS $C_P$-data series for each studied sample. The mean $C_P$ values were then taken to give the low-$T$ $C_P$ behavior for each almandine sample.

**TABLE 2.** Experimental parameters for the PPMS measurements on synthetic and natural almandine samples and derived standard entropy values

| Sample | Type | | PPMS measurement | | | | | | PPMS/DSC agreement | | |
|---|---|---|---|---|---|---|---|---|---|---|---|
| | | | Formula weight (g/mol) | Sample weight (mg) | SC* 3 K (%) | SC* 300 K (%) | $C^s/C^{add}$† 3 K | $C^s/C^{add}$† 300 K | at 298 K‡ (%) | $S^o$§ [J/(mol·K)] | $S^o$‖ corrected [J/(mol·K)] |
| R41 | sintered chip polished | 1 | 497.753 | 17.36 | 99.8 | 100 | 98 | 1.41 | –0.41 | 334.8 | 336.7 ± 0.8# |
| | | 2 | | | 99.8 | 100 | 79 | 1.37 | –0.95 | 334.1 | |
| | | 3 | | | 99.7 | 99.7 | 93 | 1.40 | –0.56 | 335.0 | |
| R22 | sintered chip polished | 1 | 497.896 | 25.85 | 99.6 | 99.4 | 216 | 2.02 | –0.92 | 334.7 | 337.8 ± 0.8# |
| | | 2 | | | 99.6 | 99.4 | 217 | 2.03 | –0.77 | 334.8 | |
| | | 3 | | | 99.7 | 99.6 | 229 | 2.06 | –0.63 | 335.1 | |
| R51 | sintered chip polished | 1 | 497.959 | 24.55 | 99.7 | 99.5 | 115 | 1.9 | –0.40 | 333.8 | 337.0 ± 0.6# |
| | | 2 | | | 99.8 | 99.7 | 178 | 2.1 | –0.23 | 334.1 | |
| | | 3 | | | 99.7 | 99.7 | 153 | 2.0 | –0.16 | 334.4 | |
| FR3 | single crystal polished | 1 | 495.789 | 29.83 | 99.2 | 99.4 | 300 | 2.41 | 0.19 | 335.4 | 337.6 ± 0.8# |
| | | 2 | | | 99.7 | 99.4 | 296 | 2.41 | 0.26 | 335.3 | |
| | | 3 | | | 99.8 | 99.7 | 350 | 2.47 | 0.79 | 336.1 | |

* SC: Sample coupling (see text for details). 3 K: value at 3 K; 300 K: value at 300 K.
† $C^s/C^{add}$: ratio of sample over addenda heat capacity at 3 K and 300 K.
‡ $100(C_P^{PPMS} - C_P^{DSC})/C_P^{DSC}$ at 298 K. $C_P^{DSC}$ is the mean of all DSC measurements made on this sample (up to three series comprising up to 5 measurements each).
§ Calculated from the raw PPMS data including 0.2 J/(mol·K) for the entropy increment from 0–3 K.
‖ $C_P$ of sintered samples was DSC-adjusted as described in Dachs and Benisek (2011). $C_P$ was corrected to almandine end-member composition for samples R22, R51 and FR3 based on garnet mole fractions given in Table 1. Corrections for impurities were performed for R22 (1 vol% hercynite) and R51 (2 vol% quartz, 1 vol% ferrosilite, 2 vol% Fe metal). Value includes 0.2 J/(mol·K) as entropy increment from 0 to 3 K.
# Error estimated as described in the text.

**Adjustment of raw $C_P$ data to account for deviation from end-member composition and for additional phases.** An adjustment of the raw $C_P$ data was also made to account for any deviation from stoichiometric end-member almandine composition. This was done for samples R22 ($X_{Alm}$ = 0.986), R51 ($X_{Alm}$ = 0.970), and FR3 ($X_{Alm}$ = 0.935) using the mole fractions of almandine (Alm), pyrope (Py), grossular (Gr), spessartine (Sp), and andradite (And) components given in Table 1 (any skiagite component and the "% remainder" were treated as andradite). For the natural almandine FR3, for example, the adjustment is expressed as

$$C_P^{Alm} = (C_P^{exp} - 0.0244C_P^{Py} - 0.0011C_P^{Sp} - 0.0394C_P^{And})/0.935 \quad (2)$$

and similarly for samples R22 and R51. The low-$T$ $C_P$ values for pyrope (Dachs and Geiger 2006), for spessartine (Dachs et al. 2009), and for andradite (Robie et al. 1987) were used in this calculation. The $C_P$ data for sample R41 required no such treatment, because it is end-member almandine within the analytical precision of the measurements (i.e., $X_{Alm}$ = 0.995 with no or very little $Fe^{3+}$).

In addition, almandines R22 and R51 contained small amounts of inclusions for which the raw $C_P$ data were also adjusted. For example, sample R22 contains ~1 vol% hercynite and sample R51 ~2 vol % quartz, ~1 vol % ferrosilite, and ~2 vol % Fe metal. $C_P$ data for these impurity phases were taken from Robie and Hemingway (1995). The minor amount, <1 vol%, of Fe-metal in sample R41 was ignored. Adjustments were made to both the PPMS and the DSC data (the raw data are given in Appendix 1[1]).

**Calculation of the standard molar entropy, $S°$.** $S°$ was calculated from the low-$T$ $C_P$ data by numerically solving the integral

$$S° - S^{T=0K} = \int_0^{298.15} \frac{C_P}{T} dT \quad (3)$$

using the Mathematica function *NIntegrate* and the function *Interpolation* for linear interpolation between data points and assuming $S^{T=0K} = 0$. The integral was evaluated over the temperature range 3 to 298.15 K and the entropy increment from 0 to 3 K was estimated as described below and amounts to 0.2 J/(mol·K). The uncertainty in $S°$ was determined by calculating $S°$ for each of the six to nine adjusted PPMS $C_P$-data series per sample and then taking the standard deviation of the various $S°$ values.

**Separation of lattice- and non-lattice contributions to $C_P$.** The molar heat capacity, $C_P$, of a substance can consist of several contributions (Grimvall 2001) and can be expressed as

$$C_P = C_{vib} + C_{mag} + C_{el} + C_{def} + ..., \quad (4)$$

where $C_{vib}$ is the vibrational or lattice contribution, $C_{mag}$ the magnetic, $C_{el}$ the electronic, and $C_{def}$ the defect contribution. In the case of almandine with $Fe^{2+}$, there is the possibility of both magnetic and electronic contributions. We assume here that defect concentrations are too minor in almandine to affect $C_P$ behavior in a significant manner [see Geiger et al. (in prep.), for a discussion on possible defect types].

To determine the vibrational heat capacity, $C_{vib}$, and to separate lattice and non-lattice contributions in the experimentally determined $C_P$ data, we employed the single-parameter phonon-dispersion model of Komada and Westrum (1997, abbreviated KW). Briefly summarized, the key feature of the KW model is that, analogous to Debye theory, a characteristic temperature, $\theta_{KW}$, is introduced and $C_P$ is expressed as a function of this single parameter. $\theta_{KW}$ can be determined by fitting the model to experimental $C_P$ data (Komada 1986; Komada and Westrum 1997; Dachs et al. 2007, 2009). An attractive feature is the behavior of $\theta_{KW}$ as a function of temperature. At temperatures above a phase transition, $\theta_{KW}$ approaches a constant value that can be used to calculate the lattice/vibrational heat capacity, $C_{vib}$, in the region of the phase transition. Any marked "drop-off" or change in the value of $\theta_{KW}$ with temperature reflects the existence of non-lattice $C_P$ contributions due to, for example, magnetic and/or electronic effects. The KW model requires various crystallographic and crystal-chemical input data, as described in Komada and Westrum (1997) or Dachs et al. (2009), and for the sake of brevity will not be repeated here.

The input values used to calculate $C_{vib}$ of almandine were the same as those used by Dachs et al. (2009) in their evaluation of the $C_P$ behavior of spessartine except for: the lattice constant $a_o$ = 11.525 Å (Geiger 1999) and $M_h$ = 38.22 g/mol, which is the arithmetic mean of the molar masses of the group of the heaviest atoms in the formula unit. The KW model gives the heat capacity at constant volume, $C_V$. The small difference between $C_P$ and $C_V$ was accounted for using the relationship $C_P - C_V = T \cdot V \cdot \alpha / \kappa$. Values for the molar volume, $V$, the thermal expansivity, $\alpha$, and the isothermal compressibility, $\kappa$, of almandine were taken from Geiger (1999). The difference between $C_P$ and $C_V$ amounts to 0.44% of $C_p$ at 298 K and becomes very small below 150 K.

## Results

### Low-temperature heat-capacity behavior and phase transitions

The PPMS measured heat-capacity values for sample R41 are shown in Figure 2 as an example (the mean of the different measurements is plotted), together with the DSC data around ambient temperature. The overlapping region between the two measurements is enlarged in the lower right inset. At low $T$'s, a prominent λ-type heat-capacity anomaly is visible at about 9 K and is attributed to a paramagnetic/antiferromagnetic phase transition (e.g., Prandl 1971; Murad and Wagner 1987; Anovitz et al. 1993).

The reproducibility of the PPMS $C_P$ measurements is, in general, very good. The mean relative differences between the three PPMS measurements performed per sample are mostly in the range 0.1 to 0.3% at $T$ > 20 K (a maximum deviation of 0.7% was observed in one case) and do not exceed 2% at $T$ < 20 K. These differences are smaller on average by 0.1% than the mean relative uncertainties (100 $\sigma_{CP}/C_P$) of the $C_P$ data (i.e., the various measurements agree within error). Sample coupling values ranged between 99.2 and 100%, indicating good thermal contact between sample and platform and thus robust $C_P$ measurements (Table 2). The almandine heat capacity contributed at least 60% to the total heat capacity at ambient $T$, as shown by the ratio $C^{sample}/C^{addenda}$ that amounts to 1.4 to 2.5 around 300 K. This value is greater at the lowest temperatures because of the heat-capacity anomalies and, thus, the sample dominates in

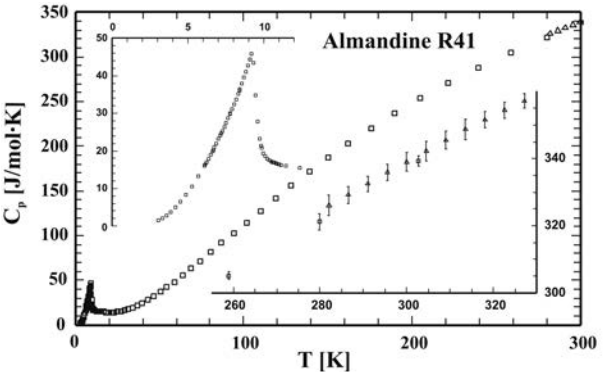


**Figure 2.** Low-temperature heat-capacity values for synthetic almandine R41. Squares represent the PPMS measurements (the mean of the three PPMS $C_P$ determinations, not DSC-adjusted, at each temperature is plotted) and triangles the DSC data around ambient $T$, where the overlapping region is shown in the lower right inset and includes ±2σ error bars. The region around the magnetic transition is enlarged in the upper left inset.

[1] Deposit item AM-12-068, Appendix. Deposit items are available two ways: For a paper copy contact the Business Office of the Mineralogical Society of America (see inside front cover of recent issue) for price information. For an electronic copy visit the MSA web site at http://www.minsocam.org, go to the *American Mineralogist* Contents, find the table of contents for the specific volume/issue wanted, and then click on the deposit link there.

this range to more than 99% of the total measured heat capacity.

The agreement between PPMS- and DSC-measured $C_P$ values around ambient $T$ is very good. PPMS-$C_P$ values for the polycrystalline samples R41, R22, and R51 are slightly lower at 298 K by 0.6, 0.8, and 0.3%, respectively, whereas in the case of the natural single-crystal platelet FR3 the PPMS-$C_P$ values are 0.4% larger compared to DSC ones.

Comparing different samples, the PPMS-$C_P$ values of all three synthetic samples R41, R22 and R51 are the same within 0.3 ± 0.2% at $T > 20$ K. Sample FR3 shows slightly larger $C_P$'s compared to the synthetics by up to ~1% at $T > 100$ K. Figure 3 shows a comparison of our $C_P$ values, in a difference plot given as $100(C_P^{\text{PPMS}}–C_P^{\text{reference}})/C_P^{\text{reference}})$, to those measured by Anovitz et al. (1993) using low-temperature adiabatic calorimetry (low-$T$AC). Between 50 and 150 K $C_P$ values are similar to within 1%. At $T > 150$ K, the $C_P$ values of Anovitz et al. (1993) are increasingly larger up to 2% compared to the PPMS-$C_P$ values for the synthetic almandines and up to 1% for the natural sample FR3. Near the magnetic λ transition around 9 K, there are measurable differences in $C_P$ behavior between our samples (Fig. 4). The temperature of the transition is a function of the $Fe^{3+}$ content in the garnet. The two essentially $Fe^{3+}$-free samples (or with very low amounts) R41 and R51 show similar $C_P$ behavior with a sharp peak at ~9.2 K. The other two samples that have ~3% $Fe^{3+}$ show $C_P$ peaks that are less pronounced and sharp and that are shifted to a lower temperature of 8.0 ± 0.2 K (Fig. 4). The almandine studied by Anovitz et al. (1993) takes an intermediate position, which is consistent with its measured $Fe^{3+}$ content of 2%.

### Standard entropy of almandine

Table 2 lists the calculated standard entropy values, $S°$, for the four studied almandine samples. They fall in the range of 333.8 to 336.1 J/(mol·K) and are similar within 0.7% in terms of the raw PPMS data. The range of $S°$ values for a given sample is even smaller, being within 0.1 to 0.3%. $S°$ calculated from adjusted $C_P$ data (only DSC adjusted for sample R41, DSC adjusted and corrected for deviation from end-member composition and for impurities for samples R22 and R51, and only corrected for deviation from the end-member composition and for impurities for FR3; see Table 2) ranges between 336.7 ± 0.8 and 337.8 ± 0.8 J/(mol·K). The final standard entropy values differ by no more than 0.3% and agree with one another excellently.

We recommend a value of $S° = 336.7 \pm 0.8$ J/(mol·K), because it derives from the "best" almandine sample R41. This value is 1.7% smaller than $S° = 342.6 \pm 1.4$ J/(mol·K) given by Anovitz et al. (1993) and the difference appears to be outside the experimental error given by both calorimetric methods. The probable reason for this is given in the discussion section.

### Non-lattice (excess) heat capacity and entropy

The non-lattice or excess heat capacity, defined as $C_{\text{ex}} = C_V–C_{\text{vib}}$, obtained by subtracting model $C_{\text{vib}}$ values from the experimental heat capacities after converting $C_p$ of almandine to $C_V$, was calculated and analyzed. Taking data from our "best" sample, R41, as an example once again, we calculated $\theta_{KW}$ as a function of temperature (Fig. 5). Above ~50 K, $\theta_{KW}$ has a constant value nearly independent of $T$ (i.e., $\theta_{\text{KW}} = 112.60 + 0.01T$) and it can be used to calculate the lattice part of almandine's heat capacity, $C_{\text{vib}}$, as function of temperature. The experimental heat-capacity values at $T > 50$ K can be described well by this $\theta_{KW}$ with a mean deviation of 0.4 ± 0.2% (Fig. 6). Below ~50 K, $\theta_{KW}$ drops off in value, because of the onset of ordering of the $Fe^{2+}$ spins that ultimately gives rise to the antiferromagnetic phase transition with a Néel temperature, $T_{\text{N}}$, of 9.2 K. The resulting excess heat capacity, $C_{\text{ex}}$, is shown in Figure 7.

For describing $C_{\text{ex}}$ behavior in the temperature region around the λ transition we used the equations (e.g., Grønvold and Sveen 1974; Dachs et al. 2007, 2009)

$$C_{\text{ex}} = \frac{A'}{\alpha'}\left[\left(\frac{|T - T_N|}{T_N}\right)^{-\alpha'} - 1\right] + B' \qquad (5a)$$

for $T < T_{\text{N}}$, and

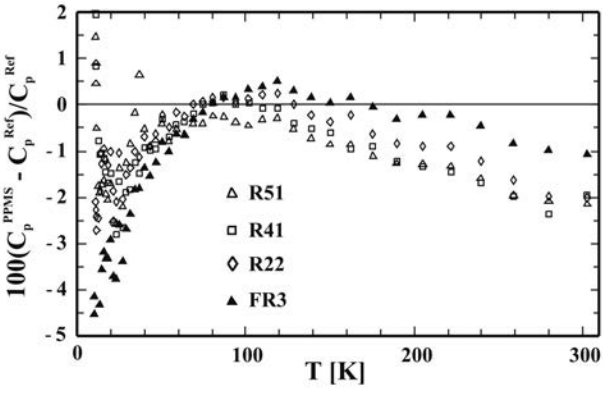


**FIGURE 3.** Difference plot of low-temperature heat capacity values for almandine from this study (samples R51, R41, R22, and FR3; $C_P^{PPMS}$) vs. that of Anovitz et al. (1993) as measured by low-$T$AC ($C_P^{Ref}$).

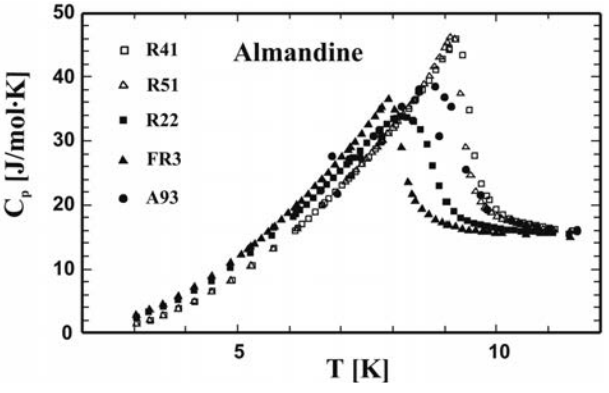


**FIGURE 4.** Heat-capacity behavior for the almandine samples of this study in the region of the magnetic phase transition around 9 K. Open squares and triangles represent the $Fe^{3+}$-free samples R41 and R51, respectively, and the solid squares and triangles the samples R22 and FR3 with 2–3% octahedral $Fe^{3+}$. The data of Anovitz et al. (1993) are shown as dots. Error bars are smaller than the symbol size.

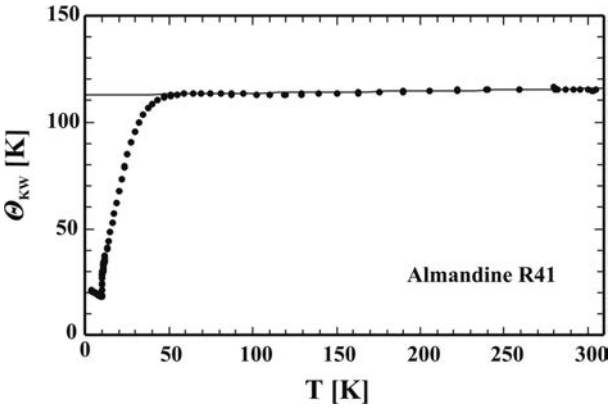


**FIGURE 5.** Characteristic temperature, $\theta_{KW}$, calculated from the experimental heat capacity of almandine R41 using the model of Komada and Westrum (1997). Above approximately 50 K, $\theta_{KW}$ approaches a nearly constant value given by $\theta_{KW} = 112.60 + 0.01T$. See text for further details.

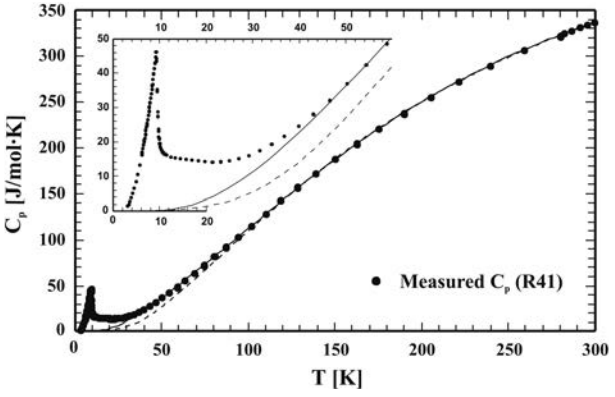


**FIGURE 6.** Vibrational heat capacity, $C_{vib}$, of almandine R41 calculated with the Komada and Westrum model (1997, solid curve) and with the Kieffer model using the vibrational spectroscopic data of Chopelas (2006, dashed curve). Above ~50 K, $C_P^{vib}$ calculated from the KW model matches the experimental heat-capacity values. The difference $C_P$-$C_V$ has been accounted for as described in the text. The inset is an enlargement in the vicinity of the magnetic phase transition.

$$C_{ex} = \frac{A}{\alpha}\left[\left(\frac{|T - T_N|}{T_N}\right)^{-\alpha} - 1\right] + B \qquad (5b)$$

for $T > T_N$. A, B, and α are fit parameters.

With Equations 5a and 5b, the low-$T$ flank of the λ anomaly and the high-$T$ side up to ~15 K can be satisfactorily fit. However, Equation 5b does not describe well the high-$T$ tail in $C_{ex}$ extending up to ~50 K. A notable feature of $C_{ex}$ in the temperature range from ~12 to 20 K is the presence of a small shoulder. We assign this to a Schottky anomaly arising from electronic transitions within the spin-orbit splitted $^5$A ground state of almandine (Geiger et al. 2003). This leads to an additional contribution, $C_{el}$, to the heat capacity since this splitting is small enough for thermal occupation of the excited state at these temperatures. Similar to Dachs et al. (2007) for the case of the forsterite-fayalite ($Fe_2SiO_4$-$Mg_2SiO_4$) solid solution, we used the expression for a two-level Schottky contribution to model $C_{el}$. We added this to Equation 5b yielding

$$C_{ex} = \frac{A}{\alpha}\left[\left(\frac{|T - T_N|}{T_N}\right)^{-\alpha} - 1\right] + B + \mathrm{R} * SF * \left(\frac{2x_1 e^{-x_1}}{(1+e^{-x_1})^2}\right) \qquad (5c)$$

for $T > T_N$, where R is the gas constant, $SF$ is a scaling factor of order 1 and $x_1 \approx 2.4\ T_{max}/T$, where $T_{max}$ is the temperature maximum of the Schottky anomaly. Using Equation 5c, $C_{ex}$ can be fit satisfactorily in the temperature region between $T_N$ and 50 K (Fig. 7). The mean deviation at $T < T_N$ is 0.7 ± 0.5% and at 10 K < $T$ < 50 K it is 0.5 ± 0.3%. The fit parameters used for the calculation are given in Table 3.

We note, though, that a unique and quantitative separation of magnetic and electronic $C_P$ contributions using Equation 5c is not possible. Different combinations of scaling factors, which determine the magnitude of $C_{el}$ and the other parameters in Equation 5c, could describe $C_{ex}$ behavior more or less equally well. For this reason we subsumed $C_{el}$+$C_{mag}$ = $C_{ex}$. In the case of spessartine garnet with $Mn^{2+}$, as compared to $Fe^{2+}$ in almandine, no Schottky anomaly was observed in the $C_P$ behavior above 2 K (Dachs et al.

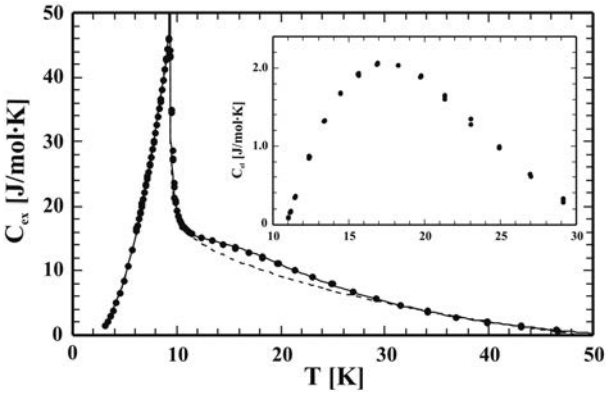


**FIGURE 7.** Excess heat capacity, $C_{ex}$, of almandine R41, as function of temperature. $C_{ex}$ is the difference between the experimental $C_P$, converted to $C_V$, and the lattice heat capacity, i.e., $C_V$–$C_{vib}$, where $C_{vib}$ was calculated with the KW model. The solid curve is a fit to $C_{ex}$ using Equations 5a and 5c in the text with the parameters given in Table 3. The shoulder in $C_{ex}$ visible around 17 K is due to an electronic heat capacity, $C_{el}$, effect or Schottky anomaly (inset). See text for further details.

**TABLE 3.** Values for the fit parameters used in Equations 5a and 5c

| Parameter | | Almandine |
|---|---|---|
| $T_N$ (K) | | 9.3 |
| $T < T_N$: | $A'$ (J/K·mol) | −23.45(22) |
| | $\alpha'$ | −0.9514(86) |
| | $B'$ (J/K·mol) | 1.66(5) |
| | $C'$ (J/K$^3$·mol) | 0.807(4) |
| $T > T_N$: | scaling factor | 1.967(6) |
| | $T_{max}$ (K) | 16.71(3) |
| | $A$ (J/K·mol) | 2.401(18) |
| | $\alpha$ | 0.3708(3) |
| | $B$ (J/K·mol) | 0.277(26) |

*Notes:* Numbers in parentheses represent one standard deviation and refer to the last digits. $T_N$: Néel temperature.

2009). Here, $C_{mag}$ above spessartine's Néel temperature of 6.2 K could be fit with Equation 5b by adding a linear and square-root term in $T$ [Dachs et al. (2009), Eq. 6b]. If this were done for the case of $C_{ex}$ of almandine, and excluding the $T$ region between 12 and 30 K, $C_{mag}$ as shown in Figure 7 (dashed curve) would result. This $C_{mag}$ behavior may be adopted to estimate the $C_{el}$ contribution given by $C_{el} = C_{ex}–C_{mag}$. $C_{el}$ amounts to a maximum of ~2 J/(mol·K) at ~17 K (Fig. 7).

The final results of this exercise in modeling the low-$T$ $C_P$ behavior of almandine are shown in Figure 8, where the experimental heat capacity values in the low-temperature range and the model $C_{vib}$ and $C_{ex}$ contributions are plotted, as well as the sum $C_{vib}+C_{ex}$. Smoothed thermodynamic functions based on these model $C_{vib}+C_{ex}$ values are given in Table 4.

Following this, the excess entropy of almandine, $S_{ex}$, was calculated by evaluating the integral $\int(C_{ex}/T)dT$ over the temperature interval 0 to 50 K using Equations 5a and 5c and the parameters given in Table 3. We obtain $S_{ex} = 33.4$ J/(mol·K) and in a similar manner we calculate $S_{el} = 1.3$ J/(mol·K). $S_{mag}$ is thus 32.1 J/(mol·K), which is 80% of the maximum possible entropy given by 3Rln5 = 40.12 J/(mol·K).

### High-temperature heat capacity and heat content of almandine

The DSC $C_P$ values are shown in Figure 9 for all almandine samples, where the mean of the DSC data are plotted after adjustment for any deviation from end-member composition and for any extra phases, as described above and in Table 2. All $C_P$ values for the various samples are very similar, so that a distinction between individual samples is not possible within the resolution shown in Figure 9. The mean relative uncertainties (i.e., 100 $\sigma_{CP}/C_P$) of the data are 0.3 ± 0.1% at $T < 650$ K for all samples. The DSC data at $T > 660$ K have a slightly larger uncertainty of 0.5 ± 0.1%. The $C_P$ values for synthetic almandines R41, R22, and R51 agree with each other within 0.4%. The $C_P$ values for natural almandine FR3 are slightly lower than the synthetics. As with the PPMS measurements, differences between individual samples are of the same order as the experimental precision of the DSC method. The $C_P$ values from Anovitz et al. (1993) are shown in Figure 9 for comparison. Their $C_P$ data between 300 and 350 K, as measured by low-$T$AC, are slightly systematically larger by 1 to 2% than our PPMS and DSC data (Fig. 9 inset). Their DSC data around 420 K agree well with the DSC data of this study, but at higher temperatures they tend to slightly lower values.

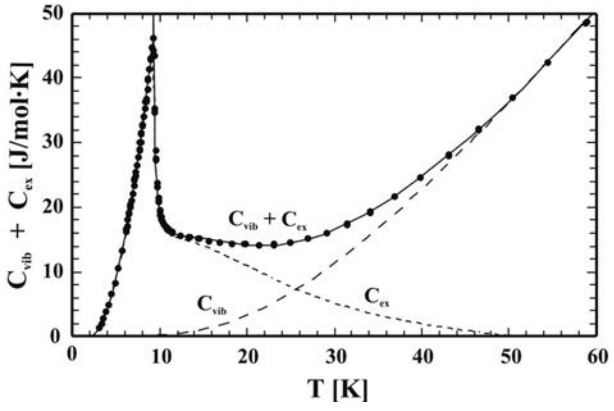


**Figure 8.** Vibrational ($C_{vib}$, long-dashed curve) and excess heat capacity ($C_{ex}$, short-dashed curve) of almandine R41 in the temperature range 0 to 60 K. The sum $C_{vib} + C_{ex}$ is shown as a solid line, the measured heat capacities as dots. See text for further details.

The heat content, $H_{965K}–H_{298K}$, of synthetic almandine was measured by Newton and Harlov (1993) giving a mean value of 305.5 ± 1.88 kJ/mol. Our measured value of $H_{1181K}–H_{302K}$ for sample FR3 is 415.0 ± 3.2 kJ/mol. We used these two heat-content values, together with the DSC data for almandine R41, and also including the PPMS data around ambient $T$, to obtain a $C_P$ polynomial for almandine at $T > 298$ K. Adopting the $C_P$ polynomial recommended by Berman and Brown (1985) and applying the method of least-squares we calculate in J/(mol·K)

$$C_P = 649.06(\pm4) – 3837.57(\pm122)\cdot T^{-0.5} – 1.44682(\pm0.06)\cdot10^7\cdot T^{-2} + 1.94834(\pm0.09)\cdot10^9\cdot T^{-3}. \quad (6)$$

This polynomial fits our DSC data with a mean deviation of 0.09 ± 0.07% and reproduces the two heat-content data $H_{965K}$-$H_{298K}$ and

**Table 4.** Smoothed molar thermodynamic functions of almandine between 3 and 298.15 K ($M$ = 497.753 g/mol)

| $T$ (K) | $C_P$ [J/(mol·K)] | $(S_T – S_0)$ [J/(mol·K)] | $(H_T – H_0)/T$ [J/(mol·K)] | Φ [J/(mol·K)] |
|---|---|---|---|---|
| 3 | 1.271 | 0.156 | 0.143 | 0.013 |
| 4 | 4.336 | 0.904 | 0.775 | 0.129 |
| 5 | 8.994 | 2.342 | 1.926 | 0.416 |
| 6 | 15.242 | 4.510 | 3.603 | 0.907 |
| 7 | 23.069 | 7.427 | 5.806 | 1.621 |
| 8 | 32.460 | 11.104 | 8.535 | 2.569 |
| 9 | 43.357 | 15.542 | 11.785 | 3.757 |
| 10 | 19.546 | 19.071 | 13.923 | 5.148 |
| 11 | 16.446 | 20.748 | 14.256 | 6.493 |
| 12 | 15.718 | 22.142 | 14.402 | 7.740 |
| 13 | 15.456 | 23.388 | 14.492 | 8.897 |
| 14 | 15.288 | 24.528 | 14.554 | 9.973 |
| 15 | 15.114 | 25.577 | 14.598 | 10.979 |
| 20 | 14.192 | 29.789 | 14.603 | 15.186 |
| 25 | 14.468 | 32.953 | 14.520 | 18.434 |
| 30 | 16.515 | 35.746 | 14.658 | 21.088 |
| 35 | 20.072 | 38.542 | 15.162 | 23.381 |
| 40 | 24.76 | 41.52 | 16.06 | 25.46 |
| 45 | 30.26 | 44.74 | 17.32 | 27.42 |
| 50 | 36.36 | 48.24 | 18.92 | 29.33 |
| 60 | 50.68 | 56.11 | 23.00 | 33.12 |
| 70 | 65.77 | 65.05 | 28.02 | 37.03 |
| 80 | 81.20 | 74.84 | 33.70 | 41.14 |
| 90 | 96.80 | 85.31 | 39.85 | 45.46 |
| 100 | 112.42 | 96.31 | 46.32 | 49.99 |
| 110 | 127.94 | 107.76 | 53.04 | 54.72 |
| 120 | 143.25 | 119.55 | 59.92 | 59.63 |
| 130 | 158.25 | 131.61 | 66.91 | 64.70 |
| 140 | 172.87 | 143.87 | 73.96 | 69.91 |
| 150 | 187.06 | 156.29 | 81.03 | 75.26 |
| 160 | 200.76 | 168.80 | 88.09 | 80.71 |
| 170 | 213.94 | 181.37 | 95.10 | 86.26 |
| 180 | 226.58 | 193.96 | 102.06 | 91.90 |
| 190 | 238.68 | 206.54 | 108.94 | 97.60 |
| 200 | 250.23 | 219.07 | 115.71 | 103.36 |
| 210 | 261.23 | 231.55 | 122.38 | 109.17 |
| 220 | 271.70 | 243.95 | 128.93 | 115.01 |
| 230 | 281.66 | 256.25 | 135.36 | 120.89 |
| 240 | 291.13 | 268.44 | 141.65 | 126.78 |
| 250 | 300.12 | 280.50 | 147.82 | 132.69 |
| 260 | 308.65 | 292.44 | 153.84 | 138.60 |
| 270 | 316.75 | 304.24 | 159.72 | 144.52 |
| 280 | 324.44 | 315.90 | 165.47 | 150.43 |
| 290 | 331.74 | 327.42 | 171.08 | 156.34 |
| 298.15 | 337.41 | 336.69 | 175.55 | 161.14 |

*Note:* $\Phi \equiv (S_T – S_0) – (H_T – H_0)/T$.

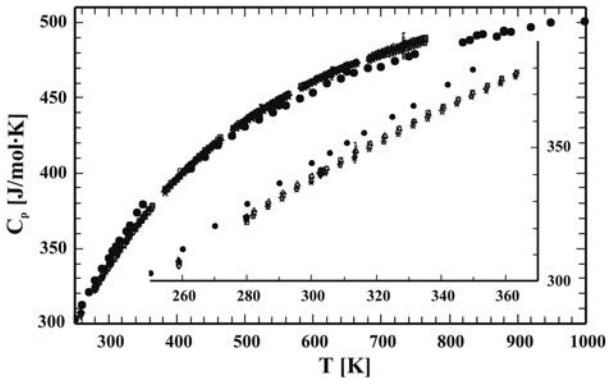


**FIGURE 9.** DSC heat-capacity values for almandine samples R41 (squares), R22 (triangles), R51 (diamonds), and FR3 (stars). The mean of the $C_P$ values per sample is plotted including the uppermost PPMS values. The data for R22, R51, and FR3 were corrected for impurities and deviation from end-member composition as described in footnote[5] to Table 2. The heat capacities measured by Anovitz et al. (1993) are plotted as dots (low-*T*AC values below 350 K and DSC values above 420 K). The $C_P$ values from the different samples of this study are so similar that the different data are only observed in an expanded plot shown from 250 to 370 K. Error bars (±2σ) are shown for only one datum per DSC series.

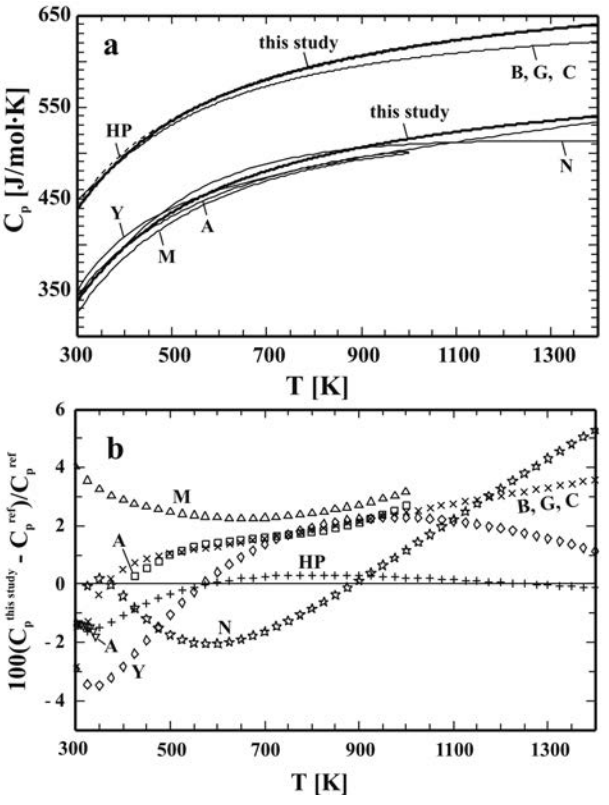


**FIGURE 10.** (**a**) Heat capacity of almandine from 300 to 1400 K given by various $C_P$ polynomials. The upper curves show $C_P$ calculated from Equation 6 and from various polynomials in different thermodynamic databases and is offset by +100 J/(mol·K) to avoid overlap. (**b**) percent difference plot showing $100(C_P^{Eq.5}–C_P^{Ref})/C_P^{Ref}$.

References: A (Anovitz et al. 1993): the squares are DSC data and the inverted triangles low-*T*AC data; M (Metz et al. 1983): Triangles; Y (Yakovlev and Vozianova 1983): Diamonds; N (Newton and Harlov 1993): Stars. Thermodynamic databases: B (Berman 1988), G (Gottschalk 1997), C (Chatterjee et al. 1998): X symbols; HP (Holland and Powell 1998, 2011): Crosses.

$H_{1181K}$-$H_{302K}$ with deviations of 0.7 and 0.1%, respectively.

Various $C_P$ polynomials proposed for almandine in the literature are compared in Figure 10a, and their differences with respect to Equation 6 are shown in Figure 10b. The polynomial in the Holland and Powell (1998, 2011) database [described as "estimated or optimized" and citing Newton and Harlov (1993) as the source] gives very similar $C_P$ values to those obtained by Equation 6 at $T > 500$ K. At $T < 500$ K, Holland and Powell's $C_P$ values are ~1.5% higher. $C_p$ polynomials in the data bases of Berman (1988), Gottschalk (1997) and Chatterjee et al. (1998), which are solely based on the DSC data of Anovitz et al. (1993), give extrapolated $C_p$ values at 1400 °C that are 3.5% lower than those given by Equation 6. The $C_P$ polynomials of Yakovlev and Vozianova (1983), Metz et al. (1983, cited in Anovitz et al. 1993), and Newton and Harlov (1993) differ by 2 to 5% compared to Equation 6.

## DISCUSSION AND APPLICATION

### Standard entropy of almandine

Our recommended $S°$ value for almandine, resulting from this calorimetric study on several different samples, is 336.7 ± 0.8 J/(mol·K). Anovitz et al. (1993) presented a value of 342.6 ± 1.4 J/(mol·K) that is 1.7% larger. It should be noted that heat capacity values in both works agree well around 100 K (Fig. 3). However, their $C_P$ values are about 2% larger than ours at 350 K, which is outside 2σ-uncertainty for the DSC-measured $C_P$ data of this study (Fig. 10b). Similar behavior was noted for $C_P$ results on grossular that were measured in the Westrum laboratory (Thiéblot et al. 1999; Dachs et al. 2012). It is possible that the adiabatic calorimetry $C_P$ data of Anovitz et al. (1993) are slightly too high around and above ambient *T*. As discussed by Andrews et al. (1978), adiabatic calorimetry in this temperature range can have experimental problems related to ensuring good thermal contact between heater, thermometer and calorimeter, as well as difficulties in maintaining adequate adiabatic-shield control. Heat-leak effects become important around and above ambient *T* (Westrum et al. 1968; Brooks and Stansbury 1988).

### Lattice and non-lattice heat capacities and entropies

Calculations of the lattice $C_P$ of almandine using the KW model give a constant value for $\theta_{KW}$ above ~50 K (Fig. 5). This can be interpreted as indicating that disordering of the magnetic moments of the $Fe^{2+}$ atoms is complete at a temperature of approximately five times greater than $T_N$. In other words, if some magnetic order was still present at $T > 50$ K, the KW model would not reproduce the experimental $C_P$ values so well. The calculated vibrational entropy is 303.3 J/(mol·K) at 298 K, which accounts for 90% of the total standard entropy, $S°$, of 336.7 J/(mol·K) at 298 K. The difference between the two, termed the excess entropy, is $S_{ex}$ = 33.4 J/(mol·K). Subtracting the estimated $S_{el}$ of 1.3 J/(mol·K) from

this latter value, one gets $S_{mag}$ = 32.1 J/(mol·K), which represents 80% of the maximum theoretically possible magnetic entropy of 40.12 J/(mol·K).

The model magnetic entropy of almandine is less than the total theoretical value. We have noted similar behavior for the case of octahedrally coordinated $Fe^{2+}$ in fayalite and for $Mn^{2+}$ in spessartine (Dachs et al. 2007, 2009). Thus, care should be exercised in simply using the theoretical magnetic contribution to estimate $S°$ for silicates containing a transition metal cation. This is normally done in various macroscopic-based entropy-estimation schemes of minerals (e.g., Holland 1989; van Hinsberg et al. 2005) and in some model lattice-dynamic calculations of crystals (see below). Adding the full magnetic entropy to a calculated $S_{vib}$ value will lead to an over estimate of $S°$ by several percent.

We also fit the experimental $C_P$ data of almandine at $T > 50$ K, using an equation containing combined Debye, Einstein, and Schottky functions (e.g., Boerio-Goates et al. 2002; Dachs and Geiger 2009; Dachs et al. 2010b), to obtain a second model $C_{vib}$. The resulting $C_{ex}$ is similar to that obtained using the KW-based model and the calculated $S_{ex}$ = 35.7 J/(mol·K) is slightly larger. The satisfactory agreement between the two different types of model calculations indicates the robustness of the obtained $C_{vib}$ and $S_{ex}$ values.

**Lattice-dynamic behavior of almandine**

There have been several previous attempts made in the literature to analyze the heat-capacity and/or lattice-dynamic behavior of almandine. In the first study, Anovitz et al. (1993) used a macroscopically based corresponding-states model that used the $C_P$ of isostructural grossular, $Ca_3Al_2Si_3O_{12}$, to obtain $C_{vib}$ of almandine from 0 to 298 K. The model gives rise to a long high-temperature "$C_P$ tail" for the magnetic phase transition at about 9 K that continues up to ~200 K. This leads to a large model $S_{ex}$ value of ~62 J/(mol·K) at 298 K. It implies the presence of some $Fe^{2+}$ spin order greatly above $T_N$ and gives a $S_{mag}$ value that greatly exceeds the theoretical value of 40.12 J/(mol·K).

The use of grossular as a "corresponding-states phase" to derive $C_{vib}$ for almandine is not without problems, as discussed by Anovitz et al. (1993). This has become even clearer following their original work, as it has been shown that there are significant differences in the bonding and vibrational behavior between the two **E**-site cations $Ca^{2+}$ and $Fe^{2+}$ in silicate garnet. This is reflected in their respective diffraction-determined atomic displacement parameters (adp), which are larger for $Fe^{2+}$ than for Ca (Geiger et al. 1992; Armbruster et al. 1992; Geiger and Armbruster 1997). The physical interpretation behind the adp values is that $Fe^{2+}$ has larger amplitudes of vibration than Ca and can be described as having dynamic disorder in the dodecahedral site of garnet [or a "rattling" type of behavior; Armbruster et al. (1992)]. From this, it has been argued further that the vibrational behavior of a given **E**-site cation is important in affecting the $C_P$ behavior of garnet at low temperatures, because atomic vibrations related to the **E**-site cations will occur at the lowest energies in the phonon density of states (e.g., Geiger 1998; Dachs and Geiger 2006; Mittal et al. 2001). For example, in the case of almandine with its heavy and smaller $Fe^{2+}$ cation, Raman-active $Fe^{2+}$-related translations occur between 171 and 256 $cm^{-1}$, whereas for grossular with its lighter and larger Ca cation Ca-related vibrations occur between 247 and 320 $cm^{-1}$ (Kolesov and Geiger 1998). This behavior is also seen in calculated partial phonon density of sites for $Fe^{2+}$ in almandine and Ca in grossular (Mittal et al. 2001), where vibrations for the former occur at lower energies than the latter. This means that $C_{vib}$ of almandine will be greater than that of grossular at low temperatures.

More serious issues have arisen in attempts to calculate the $C_P$ behavior of almandine using theoretical approaches. Gramaccioli and coworkers (Pilati et al. 1996; Gramaccioli and Pilati 2003) presented lattice-dynamic calculations for almandine. Their model $C_P$ values showed substantial differences from the experimental $C_P$ data of Anovitz et al. (1993). Thus, their $S_{vib}$ values were also less than those based on calorimetry. To obtain agreement between their model entropy values and the experimental data, they proposed that there is $Fe^{2+}$ static subsite order/disorder in almandine around the **E**-site (Wycoff postion 24*c*). They introduced, therefore, arbitrarily a $S^{conf}$ = 34.45 J/(mol·K) term, to be added to the model $S_{vib}$ values, to account for this proposed static disorder, although previously published X-ray and Raman measurements gave no evidence for any static order/disorder (Geiger et al. 1992; Armbruster et al. 1992; Kolesov and Geiger 1998).

A third approach at calculating the $C_{vib}$ behavior of almandine was made by Chopelas (2006), who used Raman and IR spectra of almandine (and other garnets as well) to obtain a model density of states. The model $C_{vib}$ values were lower compared to the experimental data of Anovitz et al. (1993) between roughly 50 and 100 K and at higher temperatures above approximately 250 K. Thus, once again, to account for differences between experiment and theory other model contributions to $C_P$ and $S°$ were discussed and introduced, including electronic, magnetic, and **E**-cation $S^{conf}$ terms.

We think that the published model lattice-dynamic calculations on almandine (as well as for spessartine and pyrope) are not capable of delivering $C_P$ and entropy values of sufficient accuracy to be used for quantitative thermodynamic calculations. We note that there is no experimental evidence to date documenting $Mn^{2+}$ or $Fe^{2+}$ static subsite disorder in either spessartine or almandine garnet [see reviews in Geiger (2004, 2008)]. The plethora of experimental results, including temperature-dependent X-ray diffraction measurements as well as EXFAS, Raman, IR, and $^{57}Fe$ Mössbauer spectroscopic measurements, is best interpreted as showing that both $Mn^{2+}$ and $Fe^{2+}$ cations have large anisotropic amplitudes of vibration (dynamic disorder) and no static disorder at or around the E-site (Geiger et al. 1992; Armbruster et al. 1992; Geiger 1998; Kolesov and Geiger 1998; Sani et al. 2004).

**Standard enthalpy of formation of almandine**

Using our calorimetric $S°$ value for almandine, we can derive a new enthalpy of formation, $\Delta H_f^\circ$, value at 298 K. To do this, we have chosen two experimentally well-determined phase equilibria

$$\text{almandine} + 3\text{rutile} = 3\text{ilmenite} + \text{sillimanite} + 2\text{quartz}, \quad (7)$$

and

$$2\text{ilmenite} = 2\text{Fe} + 2\text{rutile} + O_2. \quad (8)$$

Reaction 7 was investigated and tightly reversed by Bohlen et al. (1983) at high $P$ and $T$ and is well suited for deriving $\Delta H_f^\circ$ (Newton and Harlov 1993). Their almandine contained 2 ± 1% $Fe^{3+}$ as based on Mössbauer spectroscopic work. Other phase equilibrium studies involving almandine are less amenable for analysis, because either the almandine samples were not well characterized, or other Fe-bearing phases are involved whose standard thermodynamic properties are not well known (e.g., Harlov and Newton 1992) or because solid-solution phases are present such as, for example, hercynite (Bohlen et al. 1986). Reaction 8 was studied by O'Neill et al. (1988) electrochemically and it provides precise constraints on the thermodynamic properties of ilmenite and rutile, both of which are needed for thermodynamic calculations of reaction 7. Any non-stoichiometry of ilmenite and rutile in the experiments of O'Neill et al. was shown to be very small, if present at all.

For the experimental temperatures and pressures of reactions 7 and 8 we calculated

$$-\int_{298.15}^{T}\Delta C_{PR}\,dT + T\int_{298.15}^{T}(\Delta C_{PR}/T)\,dT - \int_{1}^{P}\Delta V_R^o\,dP = \Delta H_R^o - T\Delta S_R^o \quad (9)$$

using the $C_P$ polynomial for almandine given in Equation 6 and taking other necessary thermodynamic data from Holland and Powell (1998). The right-hand side of Equation 9 can be expressed as the matrix product $K{\cdot}D$, where $K$ is a matrix containing the stoichiometric coefficients of the $n$ different reactants in reactions 7 and 8 in the first $n$ rows ($n$ = 7) and $-T$ times the stoichiometric coefficients in the second $n$ rows. $D$ is a vector with $\Delta H_f^\circ$ and $S^\circ$ of the reactants as the components. Applying the method of least-squares, as described by Gottschalk (1997), we obtain the $\Delta H_f^\circ$ and $S^\circ$ values for almandine, ilmenite, and rutile as given in Table 5. In this treatment, $\Delta H_f^\circ$ for almandine, rutile, and ilmenite and the $S^\circ$ values for almandine and rutile could vary within the error limits placed by calorimetry. In the case of $S^\circ$ for ilmenite a weaker constraint was applied because of its larger uncertainty. O'Neill et al. (1988) recommended provisionally $S^\circ$ = 106.2 J/(mol·K), as based on their EMF results on reaction 8. This value is in good agreement with an early calorimetric determination of $S^\circ$ = 105.9 ± 1.3 J/(mol·K) (Shomate et al. 1946). A later calorimetric measurement by Anovitz et al. (1985) yielded a larger value for ilmenite of $S^\circ$ = 108.9 J/(mol·K). The $C_P$ values of Anovitz et al. (1985) are slightly larger than those of Shomate et al. (1946) being 0.7% higher at 298 K. O'Neill et al. (1988) noted that the Westrum adiabatic-calorimetry laboratory has also given a slightly larger $S^\circ$ value for fayalite of 152.4 J/(mol·K) (Essene et al. 1980) compared to the value of 151.0 J/(mol·K) measured by Robie et al. (1982). A similar situation is observed for $SrSiO_3$ and $Sr_2SiO_4$. The heat capacities of both phases, as measured by Weller and Kelley (1964) using adiabatic calorimetry, from about 150 to 300 K are slightly less than those of Huntelaar et al. (1992), as measured in the Westrum laboratory. We note these differences because they may have some bearing on the correct calorimetric value of $S^\circ$ for almandine. As discussed above, the $C_P$ values in Anovitz et al. (1993) tend to diverge from ours at approximately $T$ > 140 K with the difference increasing up to 298 K. Thus, our $S^\circ$ value is about 1.7% smaller than that measured in the Westrum laboratory.

The final calculated equilibrium positions for reactions 7 and 8 are shown in Figure 11 using the thermodynamic properties for almandine, ilmenite, and rutile in Table 5 and for the other

**TABLE 5.** Standard enthalpy of formation from the elements, $\Delta H_f^\circ$, and standard third-law entropy, $S^\circ$, of almandine, ilmenite, and rutile used to calculate the reactions almandine + 3rutile = 3ilmenite + sillimanite + 2quartz (GRAIL, Bohlen et al. 1983) and 2ilmenite = 2Fe + 2rutile + $O_2$ (IRI, O'Neill et al. 1988) shown in Figure 9 [respective properties from the Holland and Powell (1998, 2011) databases, first and second listed values, are given for comparison]

| End-member | This study | | Holland and Powell | |
|---|---|---|---|---|
| | $\Delta H_f^\circ$* kJ/mol | $S^\circ$* J/K·mol | $\Delta H_f^\circ$ kJ/mol | $S^\circ$ J/K·mol |
| Almandine | –5269.63 | 336.52 | –5263.65 | 340.0 |
| | | | –5260.65 | 342.0 |
| Ilmenite | –1232.94 | 107.51 | –1231.25 | 108.9 |
| | | | –1230.43 | 109.5 |
| Rutile | –944.09 | 50.69 | –944.19 | 50.6 |
| | | | –944.37 | 50.5 |

* Derived in this study from a least-squares treatment of the equilibrium data of GRAIL and IRI.

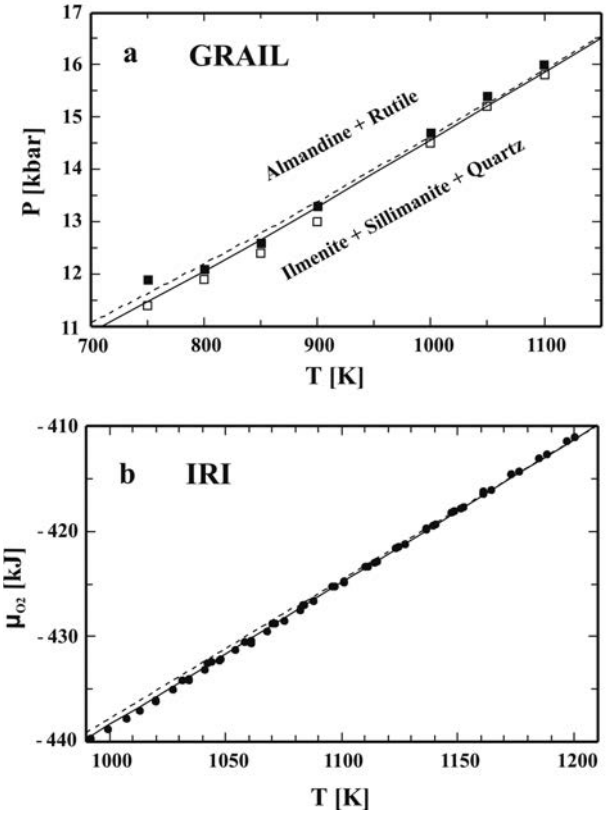


**FIGURE 11.** (**a**) $P$-$T$ position of the reaction almandine + 3rutile = 3ilmenite + sillimanite + 2quartz (GRAIL) and (**b**) chemical potential of oxygen, $\mu_{O_2}$, for the reaction 2ilmenite = 2Fe + 2rutile + $O_2$ (IRI). The experimental data used to calculate $\Delta H_f^\circ$ and $S^\circ$, given in Table 5, are shown by squares (reaction brackets determined by Bohlen et al. 1983) in **a** and by dots (EMF data of O'Neill et al. 1988) in **b**. The dashed lines are calculated using the thermodynamic properties in Holland and Powell (1998, 2011). Slightly different reaction positions are obtained from both data sets, but are not observed within the resolution of the figure.

phases using the data in the Holland and Powell database. The resulting best-fit $\Delta H_f^\circ$ value for almandine is –5269.6 kJ/mol and $S^\circ$ is 336.5 J/(mol·K). This $\Delta H_f^\circ$ is 9 kJ more negative than the value given in the most recent THERMOCALC database (Holland and Powell 2011) and is in agreement with the direct high-temperature heat of solution calorimetric determination of $\Delta H_f^\circ = -5275.8 \pm 5.7$ kJ/mol (Chattillon-Colinet et al. 1983). We calculate also for ilmenite $S^\circ = 107.51$ J/(mol·K), which is close to the value recommended by O'Neill et al. (1988), and which lies between the two values obtained via heat capacity measurements. Furthermore precise calorimetric study on well-characterized ilmenite is needed to resolve the issue of its $S^\circ$ value.

## Acknowledgments

We thank Alan Woodland for the donation of the natural almandine crystals, Gerold Tippelt for technical help, and Michael Grodzicki for helpful discussion. This work was financed by the Austrian Science Fund (FWF) through grants P21370 and P23056.

## References cited

Andrews, J.T.S., Norton, P.A., and Westrum, E.F. Jr. (1978) An adiabatic calorimeter for use at superambient temperatures. The heat capacity of synthetic sapphire ($\alpha$-$Al_2O_3$) from 300 to 550 K. Journal of Chemical Thermodynamics, 10, 949–958.

Anovitz, L.M., Treiman, A.H., Essene, E.J., Hemingway, B.S., Westrum, E.F. Jr., Wall, V.J., Burriel, R., and Bohlen, S.R. (1985) The heat-capacity of ilmenite and phase equilibria in the system Fe-Ti-O. Geochimica et Cosmochimica Acta, 49, 2027–2040.

Anovitz, L.M., Essene, E.J., Metz, G.W., Bohlen, S.R., Westrum, E.F. Jr., and Hemingway B.S. (1993) Heat capacity and phase equilibria of almandine, $Fe_3Al_2Si_3O_{12}$. Geochimica et Cosmochimica Acta, 57, 4191–4204.

Armbruster, T., Geiger, C.A., and Lager, G.A. (1992) Single crystal X-ray refinement of almandine-pyrope garnets at 298 and 100 K. American Mineralogist, 77, 512–523.

Benisek, A., Kroll, H., Cemič, L., Kohl, V., Breit, U., and Heying, B. (2003) Enthalpies in (Na,Ca)- and (K,Ca)-feldspar binaries: a high temperature solution calorimetric study. Contributions to Mineralogy and Petrology, 145, 119–129.

Benisek, A., Etzel, K., and Cemič, L. (2007) Thermodynamic mixing behavior of synthetic Ca-Tschermak-diopside pyroxene solid solutions: II. Heat of mixing and activity-composition relationships. Physics and Chemistry of Minerals, 34, 747–755.

Berman, R.G. (1988) Internally-consistent thermodynamic data for minerals in the system $Na_2O$-$K_2O$-CaO-MgO-FeO-$Fe_2O_3$-$Al_2O_3$-$SiO_2$-$TiO_2$-$H_2O$-$CO_2$. Journal of Petrology, 29, 445–522.

Berman, R.G. and Brown, T.H. (1985) Heat capacity of minerals in the system $Na_2O$-$K_2O$-CaO-MgO-FeO-$Fe_2O_3$-$Al_2O_3$-$SiO_2$-$TiO_2$-$H_2O$-$CO_2$: representation, estimation, and high temperature extrapolation. Contributions to Mineralogy and Petrology, 89, 168–183.

Boerio-Goates, J., Stevens, R., Hom, B.K., Woodfield, B.F., Piccione, P.M., Davis, M.E., and Navrotsky, A. (2002) Heat capacities, third-law entropies and thermodynamic functions of $SiO_2$ molecular sieves from $T = 0$ K to 400 K. Journal of Chemical Thermodynamics, 34, 205–227.

Bohlen, S.R., Wall, V.J., and Boettcher, A.L. (1983) Experimental investigations and geological applications of equilibria in the system FeO-$TiO_2$-$Al_2O_3$-$SiO_2$-$H_2O$. American Mineralogist, 68, 1049–1058.

Bohlen, S.R., Dollase, W.A., and Wall, V.J. (1986) Calibration and applications of spinel equilibria in the system FeO-$Al_2O_3$-$SiO_2$. Journal of Petrology, 27, 1143–1156.

Brooks, C.R. and Stansbury, E.E. (1988) Adiabatic calorimetry above 300 K. In C.Y. Ho, Ed., Specific Heat of Solids. CINDAS Data Series on Material Properties, I-2, 191–241.

Cemič, L. and Kähler, W. (2000) Calorimetric determination of the enthalpy of Mg-Fe ordering in orthopyroxene. Physics and Chemistry of Minerals, 27, 220–224.

Chatterjee, N.D., Krüger, R., Haller, G., and Olbricht, W. (1998) The Bayesian approach to an internally consistent thermodynamic database: Theory, database, and generation of phase diagrams. Contributions to Mineralogy and Petrology, 133, 149–168.

Chattillon-Colinet, C., Kleppa, O.J., Newton, R.C., and Perkins III, D. (1983) Enthalpy of formation of $Fe_3Al_2Si_3O_{12}$ (almandine) by high temperature alkali borate solution calorimetry. Geochimica et Cosmochimica Acta, 47, 439–444.

Chopelas, A. (2006) Modeling the thermodynamic parameters of six endmember garnets at ambient and high pressures from vibrational data. Physics and Chemistry of Minerals, 33, 363–376.

Dachs, E. and Benisek, A. (2011) A sample-saving method for heat capacity measurements on powders using relaxation calorimetry. Cryogenics, 51, 460–464.

Dachs, E. and Bertoldi, C. (2005) Precision and accuracy of the heat-pulse calorimetric technique: low-temperature heat capacities of milligram-sized synthetic mineral samples. European Journal of Mineralogy, 17, 251–261.

Dachs, E. and Geiger, C.A. (2006) Heat capacities and vibrational entropies of mixing of pyrope-grossular ($Mg_3Al_2Si_3O_{12}$-$Ca_3Al_2Si_3O_{12}$) garnet solid solutions: A low temperature calorimetric and thermodynamic investigation. American Mineralogist, 91, 894–906.

——— (2008) Low-temperature heat capacity of synthetic Fe and Mg-cordierite: Thermodynamic properties and phase relations in the system FeO-$Al_2O_3$-$SiO_2$-($H_2O$). European Journal of Mineralogy, 20, 47–62.

——— (2009) Heat-capacity behaviour of hemimorphite, $Zn_4Si_2O_7(OH)_2 \cdot H_2O$, and its dehydrated analogue $Zn_4Si_2O_7(OH)_2$: A calorimetric and thermodynamic investigation of their phase transitions. European Journal of Mineralogy, 21, 971–983.

Dachs, E., Geiger, C.A., von Seckendorff, V., and Grodzicki, M. (2007) A low-temperature calorimetric study of synthetic (forsterite-fayalite) {($Mg_2SiO_4$-$Fe_2SiO_4$)} solid solutions: An analysis of vibrational, magnetic and electronic contributions to the molar heat capacity and entropy of mixing. Journal of Chemical Thermodynamics, 39, 906–933.

Dachs, E., Geiger, C.A., Withers, A.C., and Essene, E.J. (2009) A calorimetric investigation of spessartine: Vibrational and magnetic heat capacity. Geochimica et Cosmochimica Acta, 73, 3393–3409.

Dachs, E., Benisek, A., and Geiger, C.A. (2010a) Relaxation calorimetry applied to mineralogical samples: Results from the Salzburg calorimetry laboratory. IUPAC International Conference on Chemical Thermodynamics 2010, Tsukuba Science City, Ibaraki, Japan; abstract CC-2202-1110S.

Dachs, E., Baumgartner, I.A., Bertoldi, C., Benisek, A., Tippelt, G., and Maresch, W. (2010b) Heat capacity and third-law entropy of kaersutite, pargasite, fluoropargasite, tremolite and fluorotremolite. European Journal of Mineralogy, 22, 319–331.

Dachs, E., Geiger, C.A., Benisek, A., and Grevel, K-D. (2012) Grossular: A crystal-chemical, calorimetric and thermodynamic study. American Mineralogist, 97, 1299–1313.

Ditmars, D.A., Ishihara, S., Chang, S.S., Bernstein, G., and West, E.D. (1982) Measurements of the relative enthalpy of pure $\alpha$-$Al_2O_3$ (NBS heat capacity and enthalpy standard reference material no. 720) from 10 to 1,950 K. Journal of Research of the National Bureau of Standards, 87, 5–9.

Essene, E.J., Wall, V.J., and Westrum, E.F. Jr., (1980) Thermodynamic properties and phase equilibria for fayalite. Geological Society of America Abstracts with Programs, 12, 422.

Geiger, C.A. (1998) A powder infrared spectroscopic investigation of garnet binaries in the system $Mg_3Al_2Si_3O_{12}$-$Fe_3Al_2Si_3O_{12}$-$Mn_3Al_2Si_3O_{12}$-$Ca_3Al_2Si_3O_{12}$. European Journal of Mineralogy, 3, 407–422.

——— (1999) Thermodynamics of $(Fe^{2+},Mn^{2+},Mg,Ca)_3Al_2Si_3O_{12}$ Garnet: An analysis and review. Mineralogy and Petrology, 66, 271–299.

——— (2004) Spectroscopic investigations relating to the structural, crystal-chemical and lattice-dynamic properties of $(Fe^{2+},Mn^{2+},Mg,Ca)_3Al_2Si_3O_{12}$ garnet: A review and analysis. In E. Libowitzky and A. Beran, Eds., Spectroscopic Methods in Mineralogy, 6, p. 589–645. European Notes in Mineralogy, Eötvös University Press, Budapest.

——— (2008) Silicate garnet: A micro to macroscopic (re)view. American Mineralogist, 93, 360–372.

Geiger, C.A. and Armbruster, T. (1997) $Mn_3Al_2Si_3O_{12}$ spessartine and $Ca_3Al_2Si_3O_{12}$ grossular garnet: Dynamical structural and thermodynamic properties. American Mineralogist, 82, 740–747.

Geiger, C.A. and Rossman, G.R. (1994) Crystal field stabilization energies of almandine-pyrope and almandine-spessartine garnets determined by FTIR near infrared measurements. Physics and Chemistry of Minerals, 21, 516–525.

Geiger, C.A., Newton, R.C., and Kleppa, O.J. (1987) Enthalpy of mixing of synthetic almandine-grossular and almandine-pyrope garnets from high temperature solution calorimetry. Geochimica et Cosmochimica Acta, 51, 1755–1763.

Geiger, C.A., Armbruster, T., Lager, G.A., Jiang, K., Lottermoser, W., and Amthauer, G. (1992) A combined temperature dependent Mössbauer and single crystal X-ray diffraction study of synthetic almandine: Evidence for the Gol`danskii-Karyagin effect. Physics and Chemistry of Minerals, 19, 121–126.

Geiger, C.A., Grodzicki, M., and Amthauer, G. (2003) The crystal chemistry and $Fe^{II}$–site properties of aluminosilicate garnet solid solutions as revealed by Mössbauer spectroscopy and electronic structure calculations. Physics and Chemistry of Minerals, 30, 280–292.

Gottschalk, M. (1997) Internally consistent thermodynamic data for rock-forming minerals in the system $SiO_2$-$TiO_2$-$Al_2O_3$-$Fe_2O_3$-CaO-MgO-FeO-$K_2O$-$Na_2O$-$H_2O$-$CO_2$. European Journal of Mineralogy, 9, 175–223.

Gramaccioli, C.M. (2002) Lattice dynamics: Theory and application to minerals. In C.M. Gramaccioli, Ed., Energy Modelling in Minerals, 4, p. 245–270. European Notes in Mineralogy, Eötvös University Press, Budapest.

Gramaccioli, C.M. and Pilati, T. (2003) Interpretation of single-crystal vibrational spectra and entropy of pyrope and almandine using a rigid-ion lattice-dynamical model. Journal of Physical Chemistry, 1007, 4360–4366.

Grimvall, G. (2001) Dependence of thermodynamic properties on atomic masses and bonding in solids. In C.A. Geiger, Ed., Solid solutions in silicate and oxide systems. European Notes in Mineralogy, 3, 11–36.

Grønvold, F. and Sveen, A. (1974) Heat capacity and thermodynamic properties of synthetic magnetite ($Fe_3O_4$) from 300 to 1050 K. Ferrimagnetic transition and zero-point entropy. Journal of Chemical Thermodynamics, 6, 859–872.

Harlov, D.E. and R.C. Newton. (1992) Experimental determination of the reaction 2magnetite + 2kyanite + 4quartz = 2almandine + $O_2$ at high pressure on the magnetite-hematite buffer. American Mineralogist, 77, 558–564.

Holland, T.J.B. (1989) Dependence of entropy on volume for silicate and oxide minerals: A review and a predictive model. American Mineralogist, 74, 5–13.

Holland, T.J.B. and Powell, R. (1998) An internally consistent thermodynamic data set for phases of petrological interest. Journal of Metamorphic Geology, 16, 309–343.

——— (2011) An improved and extended internally consistent thermodynamic dataset for phases of petrological interest, involving a new equation of state for solids. Journal of Metamorphic Geology, 29, 333–383.

Hultgren, R., Desai, P.D., Hawkins, D.T., Gleiser, M., and Kelley, K.K. (1973) Selected values of the thermodynamic properties of the elements. American Society for Metals, Metals Park, Ohio.

Huntelaar, M.E., Cordfunke, E.H.P., and Westrum, E.F. Jr. (1992) The heat capacity and derived thermophysical properties of some alkaline earth silicates and zirconates from 5 to 1000 K—I. Crystalline $SrSiO_3$ and $Sr_2SiO_4$. Journal of Physics and Chemistry of Solids, 53, 801–806.

Hwang, J.S., Lin, K.J., and Tien, C. (1997) Measurement of heat capacity by fitting the whole temperature response of a heat-pulse calorimeter. Review of Scientific Instruments, 68, 94–101.

Kolesov, B.A. and Geiger, C.A. (1998) Raman spectra of silicate garnets. Physics and Chemistry of Minerals, 25, 142–151.

Komada, N. (1986) Measurement and interpretation of heat capacities of several inorganic substances, Ph.D. Thesis. Department of Chemistry, University of Michigan, 384 p.

Komada, N. and Westrum, E.F. (1997) Modeling lattice heat capacity contributions by a single-parametric phonon dispersion approach. Journal of Chemical Thermodynamics, 29, 311–336.

Lashley, J.C., Hundley, M.F., Migliori, A., Sarrao, J.L., Pagliuso, P.G., Darling, T.W., Jaime, M., Cooley, J.C., Hults, W.L., Morales, L., Thoma, D.J., Smith, J.L., Boerio-Goates, J., Woodfield, B.F., Stewart, G.R., Fisher, R.A., and Phillips, N.E. (2003) Critical examination of heat capacity measurements made on a Quantum Design physical property measurement system. Cryogenics, 43, 369–378.

Locock, A.J. (2008) An Excel spreadsheet to recast analyses of garnet into end-member components, and a synopsis of the crystal chemistry of natural silicate garnets. Computers and Geosciences, 34, 1769–1780.

Metz, G.W., Anovitz, L.M., Essene, E.J., Bohlen, S.R. Westrum, E.F. Jr., and Wall, V.J. (1983) The heat-capacity and phase equilibria of almandine. EOS, 64, 347–347.

Mittal, R., Chaplot, S.L., Choudhury, N., and Loong, C.-K. (2000) Inelastic neutron scattering and lattice-dynamics studies of almandine $Fe_3Al_2Si_3O_{12}$. Physical Review B, 61, 3983–3988.

Mittal, R., Chaplot, S.L., and Choudhury, N. (2001) Lattice dynamics calculations of the phonon spectra and thermodynamic properties of the aluminosilicate garnets pyrope, grossular, and spessartine $M_3Al_2Si_3O_{12}$ ($M$ = Mg, Ca, and Mn). Physical Review B, 64, 094302.

Mraw, S.C. (1988) Differential scanning calorimetry. In Cy. Ho, Ed., Data series on material properties, 1-2. Hemisphere Publishing Company, New York, pp. 395–437.

Murad, E. and Wagner, F.E. (1987) The Mössbauer spectrum of almandine. Physics and Chemistry of Minerals, 14, 264–296.

Newton, R.C. and Harlov, D.E. (1993) The thermodynamic properties of almandine. Canadian Mineralogist, 31, 391–399.

O'Neill, H.St.C., Pownceby, M.I., and Wall, V.J. (1988) Ilmenite-rutile-iron and ülvospinel-ilmenite-iron equilibria and the thermochemistry of ilmenite ($FeTiO_3$) and ülvospinel ($Fe_2TiO_4$). Geochimica et Cosmochimica Acta, 52, 2065–2072.

Pilati, T., Demartin, F., and Gramaccioli, C.M. (1996) Atomic displacement parameters for garnets: A lattice-dynamical evaluation. Acta Crystallographica, B52, 239–250.

Prandl, W. (1971) Die magnetische Struktur und die Atomparameter des Almandins $Al_2Fe_3(SiO_4)_3$. Zeitschrift für Kristallographie, 134, 333–343.

Robie, R.A. and Hemingway, B.S. (1995) Thermodynamic properties of minerals and related substances at 298.15 K and 1 bar ($10^5$ Pascals) pressure and at higher temperatures. U.S. Geological Survey Bulletin 2131, 461 p.

Robie, R.A., Finch, C.B., and Hemingway, B.S. (1982) Heat capacity and entropy of fayalite ($Fe_2SiO_4$) between 5.1 and 383 K. Comparison of calorimetric and equilibrium values for the QFM buffer reaction. American Mineralogist, 67, 463–469.

Robie, R.A., Zhao, B., Hemingway, B.S., and Barton, M.S. (1987) Heat capacities and thermodynamic properties of andradite garnet, $Ca_3Fe_2Si_3O_{12}$, between 10 and 1000 K and revised values for $\Delta_f G^\circ_m$ (298.15 K) of hedenbergite and wollastonite. Geochimica et Cosmochimica Acta, 51, 2219–2224.

Sani, A., Quartieri, S., Boscherini, F., Antonioli, G., Feenstra, A., and Geiger, C.A. (2004) Atomistic-scale structural and dynamic properties of almandine-spessartine solid solutions: An XAFS study at the Fe and Mn $K$-edges. European Journal of Mineralogy, 16, 801–808.

Shomate, C.H., Naylor, B.F., and Boericke, F.S. (1946) Thermodynamic properties of ilmenite and selective reduction of iron in ilmenite. U.S. Bureau of Mines Report Inv. 3864.

Thiéblot, L., Téqui, C., and Richet, P. (1999) High-temperature heat capacity of grossular ($Ca_3Al_2Si_3O_{12}$), enstatite ($MgSiO_3$), and titanite ($CaTiSiO_5$). American Mineralogist, 84, 848–855.

van Hinsberg, V.J., Vriend, S.P., and Schumacher, J.C. (2005) A new method to calculate end-member thermodynamic properties of minerals from their constituent polyhedra II: Heat capacity, compressibility and thermal expansion. Journal of Metamorphic Geology, 23, 681–693.

Weller, W.W. and Kelley, K.K. (1964) Low-temperature heat capacities and entropies at 298.150 K of crystalline silicates of barium and strontium. U.S. Department of the Interior, Bureau of Mines, 6556, 8 p.

Westrum, E.F. Jr., Furukawa, G.T., and McCullough, J.P. (1968) Low-temperature Calorimetry. In J.P. McCullough and D.W. Scott, Eds., Experimental Thermodynamics, Volume I, Calorimetry of Non-Reacting Systems. International Union of Pure and Applied Chemistry, Plenum Press, New York, p. 133–214.

Woodland, A.B., Droop, G., and O'Neill, H.St.C. (1995) Almandine-rich garnet from near Collobrieres, southern France, and its petrological significance. European Journal of Mineralogy, 7, 187–194.

Yakovlev, B.G. and Vozianova, O.V. (1983) The thermodynamic parameters of almandine. Geochemistry International, 20, 50–61.

Zherebetskyy, D., Lebernegg, S., Amthauer, G., and Grodzicki, M. (2012) Magnetic structure of almandine. Physics and Chemistry of Minerals, 39, 351–361.

Manuscript received March 9, 2012
Manuscript accepted June 26, 2012
Manuscript handled by Daniel Harlov